Recovering the free-surface dynamics of shallow turbulent flows using Digital Image Correlation (DIC)

Michael-David Johnson, Fabio Muraro, Simon J. Tait, Giulio Dolcetti & Anton Krynkin
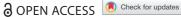
Published online: 08 Oct 2025.

Submit your article to this journal ⬀

Article views: 180

View related articles ⬀

View Crossmark data ⬀

International Association
for Hydro-Environment
Engineering and Research

Hosted by
Spain Water and IWHR, China

Taylor & Francis
Taylor & Francis Group

RESEARCH PAPER

&OPEN ACCESS   Check for updates

Recovering the free-surface dynamics of shallow turbulent flows using Digital Image Correlation (DIC)

Michael-David Johnson[a], Fabio Muraro [a], Simon J. Tait [a], Giulio Dolcetti[b] and Anton Krynkin[a]

[a]School of Mechanical, Aerospace and Civil Engineering, University of Sheffield, Sheffield, UK; [b]Department of Civil, Environmental and Mechanical Engineering, University of Trento, Trento, Italy

ABSTRACT

Numerous studies on free-surface behaviour of turbulent flows have described it as a complex phenomenon composed of different moving features. No agreement exists as to which water surface features are expected for specific flow conditions in a channel with a rough bed. There is practical difficulty in capturing the dynamic nature of the surface with sufficient accuracy and resolution. This paper describes a series of experiments for a range of conditions over two bed topographies, in which Digital Image Correlation (DIC) was used to capture surface elevation data. Frequency–wavenumber analysis highlighted a range of disturbances assumed to be created by features of the turbulent flow. Surface wave patterns were observed to change with flow condition and indicated sensitivity to the bed arrangement. This indicated that DIC can be an appropriate method in studies that wish to examine the mechanics of surface behaviour in open channel turbulent flows.

1. Introduction

Recent studies have indicated that free-surface deformations of turbulent channel flows can be caused by a variety of physical phenomena found in laterally and depth-sheared flows. A consensus on the main mechanisms behind the generation of the free-surface wave patterns has yet to be reached (Muraro et al., 2021). Brocchini and Peregrine (2001) suggested that the interactions between the water surface and the underlying turbulence-driven structures are expected to produce a wide variety of water surface patterns (e.g. vortex dimples, scars and boils). Smolentsev and Miraghaie (2005) and Nichols et al. (2016) proposed that the free-surface wave patterns might be the result of the interaction between coherent structures generated in the flow and the air–water interface. Surface deformations forced by turbulent pressure fluctuations can transition to freely propagating gravity-capillary waves once the forcing stops (Teixeira & Belcher, 2006). In shallow flows, gravity-capillary waves are also forced by the bed roughness acting as a fixed disturbance (Dolcetti et al., 2016; Gakhar et al., 2020), generating both stationary and propagating waves that can further interact with turbulent structures (Dolcetti & García Nava, 2019; Luo et al., 2023). Turbulence-forced surface patterns and gravity-capillary waves are therefore believed to be representative of different processes. Measuring and understanding the behaviour of both are necessary for

the interpretation of the mutual interaction between the flow and the free surface. The combination of these different wave types can produce a complex and dynamic three-dimensional (3D) surface wave pattern that can be difficult to measure and interpret.

A separation between the two types of surface features can be obtained by means of a Fourier transform in space and in time of water surface elevation data, e.g. the frequency–wavenumber spectrum (Dolcetti et al., 2016; Savelsberg & Van De Water, 2009). Turbulence-forced surface deformations travel approximately at the surface flow velocity, while gravity-capillary waves travel in all directions, propagating relatively to the flow at their own speed, which depends on their wavelength and flow depth. This difference in propagation velocity results in distinct dispersion relationships that can be identified in the observed frequency–wavenumber spectra.

However, the estimation of frequency–wavenumber spectra requires a simultaneous characterization of the water surface in space and in time, which can be difficult to achieve with sufficiently high accuracy and spatial and temporal resolution for many practical situations. This requirement justifies the need for water surface measurement techniques able to collect high resolution water surface elevation data that precisely characterize the 3D form and dynamics of such water interfaces, and so permitting robust frequency–wavenumber spectra to be obtained.

CONTACT Anton Krynkin ✉ a.krynkin@sheffield.ac.uk

Savelsberg and Van De Water (2009) and Dolcetti et al. (2016) determined the frequency–wavenumber spectra of the water surface elevation along the streamwise and lateral direction separately using a scanning laser beam and an array of conductance wave gauges, respectively. 1D spectra are difficult to interpret since the contributions of all waves with the same projection of the wavenumber vector along the measurement direction collapse onto a single point regardless of their actual wavenumber modulus. This strongly limits the characterization of the surface features due to the marked three-dimensionality of the surface patterns and because of the lack of symmetry caused by the advection by the flow in the streamwise direction (Dolcetti et al., 2016). Dolcetti and García Nava (2019) managed to estimate the frequency wavenumber spectra in three dimensions by applying a wavelet spectral method (Donelan et al., 1996) to a group of discrete wave gauges arranged in transects in the streamwise and lateral directions. However, the resulting spectra had limited resolution. Smeltzer et al. (2019) employed a synthetic Schlieren method to reconstruct the evolution of the surface shape in time and calculated its frequency–wavenumber spectrum. Their flow conditions, however, were not representative of typical shallow turbulent free surface flows due to a relatively small flow velocity to gravity wave velocity. Also, their surface measurement method is not easily applicable to practical channel flows over a rough bed. Luo et al. (2023) combined a decomposition of the simulated surface deformation patterns based on the frequency–wavenumber spectrum with a proper orthogonal decomposition of the simulated turbulent flow field to highlight the complex interactions between turbulence and the free surface for a flow behind a backward-facing step simulated via a large eddy simulation. This demonstrated the potential for rigorous surface decomposition to provide an improved fundamental understanding of turbulent flow behaviour.

It is therefore of importance to identify a suitable experimental technique that is able to provide high-resolution data resolved in space and in time while minimizing the disturbance to the flow and without impairing the characterization of the velocity field below the water surface. Non-contact water surface measurement techniques fit such requirements. In general, these techniques can be based on optical, acoustic or radio approaches. Acoustic methods have already been used to locally reconstruct a dynamic air–water interface or to derive areal surface properties such as mean roughness height, frequency–wavenumber spectra and mean surface velocity (Dolcetti et al., 2024; Fukami et al., 2008). For similar purposes, Walsh et al. (1985) and Welber et al. (2016) used radio waves, while Gharib and Weigand (1996) and Turney et al. (2009) made use of optical methods. Each method has comparative

advantages and disadvantages. For example, for acoustic and radio methods, the free surface represents a very good reflecting surface due to the higher impedance of water than air (Nichols et al., 2013). The same advantage, however, does not apply for optical techniques as the identification of the transparent water free surface can be affected by the presence of the underlying bed topography. To prevent this interference, optical methods require specific illumination and/or cameras positioning or even opaque water (Cobelli et al., 2009; Tsubaki & Fujita, 2005). On the other hand, optical methods are more practical in the field due to the facility of the calibration procedure and adaptability.

The use of different optical technologies to measure the shape of the surfaces is well established in various fields (Guidi et al., 2014; Vandenberghe et al., 2001). Descriptions and characteristics of these methods can be found in the reviews of Jähne et al. (1994) and Pan (2018). Among the numerous optical techniques, Digital Image Correlation (DIC) (Peters & Ranson, 1982) is one of the most popular. This is because DIC can robustly reconstruct a solid surface and can operate with flexibility (Pan, 2018; Pan et al., 2009). The complete theory behind image correlation is lengthy and, on this purpose, Chu et al. (1985) provides an excellent description of the DIC method. However, to briefly describe the principles of DIC, it can be said that this techniques relies on the idea that an object reflects light differently according to its deformation state. If this holds true, the deformation field can be derived by comparing the different light intensity values (Chu et al., 1985). Illumination information carried by a single pixel, however, is not enough to produce a unique signature and groups of neighbour pixels (named 'subsets' or 'facets') need to be considered. Often, to improve the uniqueness of a facet, random patterns are created on the surface of the target (Pan, 2011). Cross-correlation is later performed among these facets to obtain the instantaneous surface profile.

DIC has typically been used to measure both static and slowly evolving solid surfaces, though few studies have measured the dynamic liquid surface of open-channel flows (Nichols et al., 2020; Wu et al., 2022). An approach to measure the dynamics of the water surface of a turbulent open-channel flow employing DIC is presented here. The aim of the study was to assess whether DIC could be used to recover sufficiently high quality information on a dynamic air–water interface to ensure that the different types of surface waves could be separated and identified. This would allow the in-depth study of the underlying physical processes in free-surface turbulent flows over man-made and natural channels using a non-contact measurement technique that can be deployed without the need to change the opaqueness of the water. The study used DIC data

from a series of controlled laboratory flume experiments combined with analytical models to test whether a DIC based measurement system could be usefully employed in this field.

The following pages are organized as follows: Section 2 describes the instrumentation used for this investigation, the characteristics of the flow conditions tested and the data processing procedure that was implemented; Section 3 presents the mathematical model against which the data was compared with; Section 4 critically discusses the results obtained from this series of tests; Section 5, finally, draws some conclusions on the observed data patterns and on the capability of DIC to be used as a technique for surface monitoring.

2. Experimental equipment, arrangement and test procedure

Two series of steady and uniform flow experiments employing different bed arrangements were performed in a tilting recirculating glass-walled rectangular flume. The flume has a working length of 15 m and a width, W, of 0.503 m. The inlet tank contains porous elements to minimize any transient effects produced by the re-circulation pump, while the outlet has an adjustable gate to ensure uniform flow conditions in the working length of the flume.

The flume bed was covered from the inlet to a location 4.80 m downstream with well sorted river gravel having a nominal size of 20 mm to encourage the development of a stable turbulent boundary layer. The remaining length of the flume bed contained a layered bed arrangement of plastic spheres and sand to simulate a stable flat river bed with a geometrically well described surface (spheres), but which had an inherent vertical porosity variation (sand) as found in natural gravel river beds (Figure 1). In this study, the 24.7 mm diameter spheres were organized in two different surface packing arrangements, termed A and B (Figure 2). Pattern A was a hexagonally-packed arrangement having peak to peak planes oriented along the streamwise direction, whilst the B arrangement was again a hexagonally-packed arrangement but had peak to peak planes aligned along the spanwise direction. The elevation distribution of Packing B was statistically identical to packing A. These arrangements provided stable surfaces but different surface orientations in relation to the main direction of the flow. Sand with a narrow grain size distribution (99% of its mass distributed between 600 and 850 μm) was used to fill the gaps between spheres in order to produce a vertical porosity profile from the top to the base of the spheres that resembles the vertical porosity profile observed in natural river gravel deposits. These beds were placed in the flume which was then tilted to have a slope of 1/500.

Before each series of tests over a different bed arrangement, the discharge was progressively increased up to $25\,l\,s^{-1}$ and held steady for 12 h. At this flow rate, the boundary shear stress was enough to remove all the excess of sand, revealing the bed texture created by the packed spheres. This process of water-working also allowed the consolidation of the sand and the creation of a complex but stable bed structure for the subsequent tests. At the end of this procedure, the bed resulted in hemispheres emerging from a permeable sand layer.

Two series of experiments were conducted over the two beds. The hydraulic characteristics of each flow condition are reported in Table 1. The controlling parameters of each experiment were determined based on the measured depth- and time-averaged velocity, $\bar{U}_B$ (defined as the ratio between the flow rate Q and the liquid cross-sectional area $A = Wd$, where d is the water depth) and on the time-averaged surface velocity, $\bar{U}_S$. For gravity-capillary waves, a particular wavelength exists for which the dispersion component governed by gravity is balanced by the dispersion produced by capillarity. For this wavelength, a minimum phase velocity occurs. Lamb (1945) found this minimum value to be equal to $0.23\,m\,s^{-1}$ for the air–water interface. With this threshold value in mind, it was decided to have a test with flow conditions with both $\bar{U}_B$ and $\bar{U}_S$ below $0.23\,m\,s^{-1}$, one flow condition where $\bar{U}_B$ was below and $\bar{U}_S$ was above the threshold value and three flow conditions with both velocities above the minimum phase velocity for each bed configuration. The experimental hydraulic conditions were designed to evaluate the free-surface behaviour, the different wave generation mechanisms and the change they may experience for progressively higher velocities. It was expected that for these flow conditions different mixtures of turbulence-forced surface deformations and gravity-capillary waves would be observed. The flow conditions had aspect ratio (ratio between flume width and flow depth, calculated from the top of the bed spheres) between 5.2 and 25.4, and relative submergence (ratio between flow depth and diameter of the spheres) between 1.5 and 10.5. These values were described by Robert (1990) and Ferguson (2007) as typical for flow conditions observed in natural gravel bed rivers.

The water surface behaviour was investigated using a DIC system positioned at the location 9.4 m from the inlet (4.6 m downstream from the beginning of the test bed, corresponding to 232 to 59 times the experimental water depths). The DIC system was formed by two Imager MX 4M cameras (LaVision, Biceste, UK) (2048 × 2048 pixel, 5.5 μm size pixel) mounting Tamron (Tamron, Japan) M112FM16 lenses (16 mm focal length, f/2.0). The cameras were placed in a line along the flume centreline 0.40 m above the bed and a distance 0.70 m from each other (Figure 3). The cameras
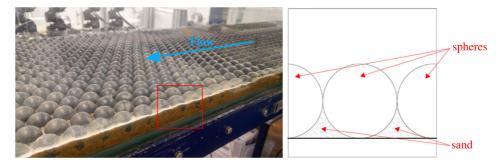
Figure 1. (a) Composite bed made of spheres embedded in sand. (b) Sketch of the composite bed.
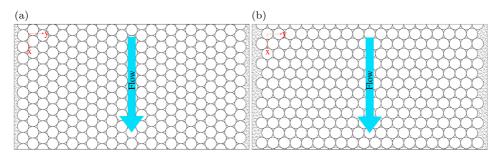

Figure 2. (a) Arrangement A: hexagonally-packed with sphere peak to peak planes aligned with the streamwise flow direction. (b) Arrangement B: hexagonally-packed with sphere peak to peak planes aligned with the spanwise direction.

were secured onto a stiff mounting bar that was physically isolated from the flume to ensure that any vibrations produced during the tests with flowing water did not impact on the quality of the DIC measurements. The camera mounting bar was set to be parallel to the flume bed so that the DIC measurement values formed a plane parallel to the time and space averaged water surface and flume bed. During the different tests the cameras' position was fixed, but because of the different flow conditions the distance free surface to cameras ranged between 462 mm and 516 mm. This caused the field of view (FOV) to range in size from a square of dimensions 363 mm to 325 mm and the spatial resolution of the collected images to vary between 0.16 and 0.18 mm/pixel. The lens aperture was set at f/16 to produce a depth of field as wide as possible and so have as much as possible of the FOV in reasonable focus. Illumination was provided by two blue LED arrays shining from above the cameras. These LEDs were positioned

0.6 m above the bed without obstructing the cameras' view. The area of the LEDs is $350 \times 250 \, \text{mm}^2$ (streamwise and spanwise). Considering a divergence angle of $8°$ for the light emitted by the LEDs, an area of $518 \times 418 \, \text{mm}^2$ was illuminated in correspondence of the bed level.

To allow the reconstruction of the instantaneous free-surface profile using the DIC system, cenospheres (POS-IBW 300 produced by Possehl Erzkontor GmbH, Lübeck, Germany) were used as small floating tracers to identify the water surface in the collected images. Cenospheres are ceramic hollow spheres which float due to their low density ($\rho_{cs} = 700 \, \text{kg m}^{-3}$). They also create a light speckle pattern of particle groupings on the free surface, allowing the surface reconstruction algorithm within the DIC system to create facets, the temporal deformation of which was used to quantify the surface deformation. Compared to other buoyant surface tracer candidates (e.g. hollow glass spheres

Table 1. Characteristics of the flow conditions tested.

Test	Q (l s^{-1})	$\bar{U}_B$ (m s^{-1})	$\bar{U}_S$ (m s^{-1})	d (mm)	Re	F	A_R	σ_{DIC} (mm)	σ_{WP} (mm)
FC1A	1.4	0.14	0.18	19.8	2800	0.32	25.4	0.074	0.115
FC2A	3.3	0.2	0.26	33.1	6500	0.35	15.2	0.108	0.147
FC3A	10.5	0.33	0.43	64.1	20,700	0.41	7.8	0.313	0.277
FC4A	15.7	0.38	0.47	81.6	30,900	0.43	6.2	0.399	0.378
FC5A	21.1	0.43	0.53	97.5	41,500	0.44	5.2	0.643	0.576
FC1B	1.93	0.19	0.23	20.7	4100	0.41	24.3	0.081	0.145
FC2B	3.53	0.23	0.31	30.7	7700	0.42	16.4	0.125	0.158
FC3B	10.84	0.35	0.45	61.5	24,200	0.45	8.2	0.582	0.537
FC4B	15.85	0.41	0.51	76.7	34,700	0.47	6.6	0.712	0.649
FC5B	21.56	0.47	0.58	91.9	47,400	0.49	5.5	0.591	0.544

Note: Q is discharge; $\bar{U}_B$ is time- and depth-averaged velocity; $\bar{U}_S$ is average surface velocity; d is water depth; Re is Reynolds number (Re $= \bar{U}_B d / \nu$, where ν is the kinematic viscosity of water); F is Froude number (F $= \bar{U}_B / (gd)^{0.5}$ where g is gravitational acceleration); A_R is aspect ratio, σ_{DIC} and σ_{WP} are the standard deviations of the free-surface elevation measured via DIC and conductance wave probe, respectively.
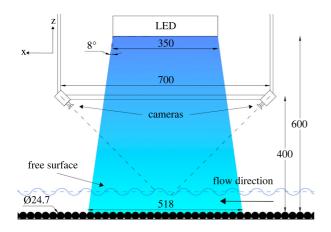
Figure 3. Schematic of the DIC cameras and illumination setup (dimensions in mm). The cameras were positioned directly above the water surface on a stiff frame that was parallel with the water and bed slope. The LED illumination was placed in the centre of the measurement area above the cameras.

and silver-coated hollow glass spheres), electrostatic interactions between discrete elements do not occur. The main consequence is that particles do not lump, so that surfactants are not needed. Cenospheres are hydrophilic and do not adhere to the water–air interface, suggesting that they do not affect the surface tension (Turney et al., 2009). The cenospheres were first sieved to isolate the fraction with particle diameters below 300 μm. This value was chosen as for diameters larger than 300 μm the Stokes number, St, became greater than 0.1. The Stokes number, defined as the ratio between the particle and fluid characteristic time scales, is used to verify the capability of a particle to follow the flow without disturbing it (Akutina, 2016). Tropea et al. (2007) suggested tracers having $St < 0.1$ are able to correctly describe the flow path with an accuracy error below 1%. As the sieved material used in the tests was characterized by a range of diameters between 90 and 280 μm, the observed Stokes numbers were always below the 0.1 threshold.

All the experiments were carried out following the same procedure. Before starting a test, a calibration plate was placed at the expected streamwise, lateral and vertical position of the air–water interface and the camera positions were physically adjusted to aim at the same location. A calibration image data set for the cameras was obtained by taking 40 in-focus images of the calibration plate set at slightly different heights and inclinations.

After the calibration images had been collected, the flow discharge was slowly increased to the desired value and the flume outlet gate was adjusted to ensure the establishment of uniform flow conditions. Sixty minutes after the discharge and gate position were set, images were collected at a frequency of 100 Hz in 300 s long acquisitions. DIC data sets consisted of time series containing 30,000 images. To produce the

free-surface coating necessary for the DIC algorithm to work, cenospheres were introduced concurrently in different ways. Pumped surface skimmers were positioned on the water surface inside the flume storage tank to collect the previously circulated tracers and recirculate them via the main pump. Peristaltic pumps were also used to introduce a mixture of water and cenospheres just below the free surface at the flume inlet position. Finally, dry cenospheres were manually sprinkled from above in correspondence with the transition between gravel and composite bed (i.e. 4.80 m from the inlet). Uniformly coating the free surface was more challenging for progressively higher flow rates and depths because of stronger secondary flows and of larger and more frequent coherent structures causing the renewal of the free surface, resulting in areas of the water surface with few cenospheres. Nonetheless, a sufficiently high level of surface coating was achieved (especially at low flow rates), allowing the DIC algorithm to reconstruct enough of the free-surface shape for later water surface analysis (Figure 4). Once the images were acquired, uniform flow conditions were verified again by taking water depth measurements along the flume with a streamwise spacing of 30 cm and used to confirm, via linear interpolation that the water slope was the same as the bed slope. As a last step, small buoyant objects were released at position 4.80 m and the time required for them to travel between two distinct sections was measured for 20 times. This allowed an estimate for the average and standard deviation of the free-surface velocity to be obtained.

To obtain the instantaneous shape of the free surface the raw images were firstly processed using the Strain toolbox provided with DaVis by LaVision (Bouguet, 2000; Fleet & Weiss, 2006). The images were subdivided in 21 pixel-wide facets and the step size (displacement of the interrogation window) was set to 13 pixels, resulting in a spatial resolution varying between 1.5 and 2.2 mm according to the water depth. Facet and step sizes were chosen as these values were seen to be optimal between spatial accuracy and uniqueness of the speckle pattern created by the floating cenospheres. The reconstructed instantaneous surface height, however, presented deviations from the mean water level. This occurred because the calibration plate was not perfectly aligned with the expected position of the water surface when taking the first image of the plate which defined the reference system. To compensate this anomaly, the time series for the reconstructed height at each location were time-averaged over the entire duration. The resulting time-averaged height field, representing the spatial trend inherited from the plate misalignment during the calibration procedure, was later subtracted from the corresponding instantaneous height field data to obtain the surface fluctuations around a mean water level that was now set to a value of 0 mm.
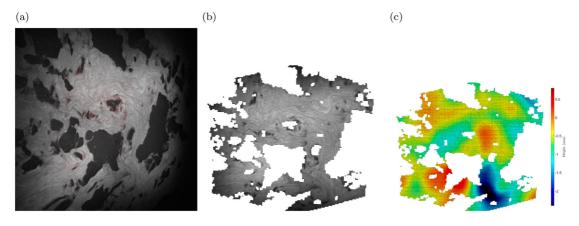
Figure 4. Processing sequence for a frame extracted from flow condition FC5B. (a) Raw camera image (b) Orthorectified free surface. (c) Reconstructed free-surface height field.
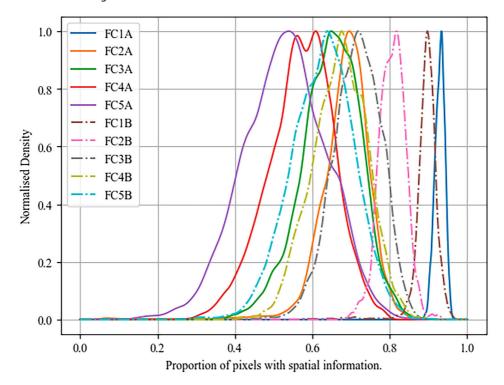

Figure 5. Normalized kernel density estimation of proportion of pixels in the images that contain surface elevation information for all measurements. The normalization was done by the division of the maximum value.

To evaluate the stationarity of the water surface fluctuation field, an augmented Dickey–Fuller test was conducted on the data. However, due to the large size of the time series, it was not possible to run the test over the entire 5min long data collection period. For this reason, each data set was subdivided into five 60s long and into two 150s long segments before conducting the test on each sub-dataset. In all the cases, the test rejected the null hypothesis, implying the stationarity of the time series. The standard deviation was also calculated for each segment to observe the variation across the DIC data set. Together with the reconstructed surface height, the instantaneous stereo reconstruction error field was produced which was used to calculate the in-plane uncertainty. For all the tests, the average triangulation error was less than 0.075 pixels, corresponding to 0.01 mm.

The vertical surface elevation uncertainty was evaluated by comparison with data from a conductance wave probe located near the camera's field of view (Muraro, 2024). Wave probe measurements were conducted without cenosphere shortly before the DIC measurements. The standard deviations of the surface elevation measured with the two methods are shown in Table 1. In the lower flow conditions FC1 and FC2, DIC underestimated the surface elevation by up to 47% and 27%, respectively. This could be due to the high density of cenospheres, causing significant particle–particle interactions. In the remaining higher flow conditions, these interactions appeared to be negligible and the two methods agreed within a 10 % difference. It is noted that wave probes are an intrusive instrument, which can also be affected by significant uncertainties.

Table 2. Spatial information of the flow conditions tested.

Test	L_ω (rad s^{-1})	L_{k_x} (rad m^{-1})	L_{k_y} (rad m^{-1})	S_ω (rad s^{-1})	S_{k_x} (rad m^{-1})	S_{k_y} (rad m^{-1})	Shape
FC1A	314.16	1948.4	1948.4	0.02	19.0	18.5	(205 211 29999)
FC2A	314.16	1903.4	1903.4	0.021	19.7	18.0	(193 211 29999)
FC3A	314.16	1931.1	1931.1	0.022	21.7	17.5	(178 221 28089)
FC4A	314.16	1948.4	1948.4	0.021	22.7	17.9	(172 218 29999)
FC5A	314.16	2084.3	2084.3	0.025	21.1	17.4	(198 240 25483)
FC1B	314.16	1760.1	1760.1	0.021	17.5	16.1	(201 218 29999)
FC2B	314.16	1558.8	1558.8	0.023	19.1	14.8	(163 211 26770)
FC3B	314.16	1708.3	1708.3	0.021	19.9	15.3	(172 224 29999)
FC4B	314.16	1742.6	1742.6	0.021	20.7	15.0	(168 232 29999)
FC5B	314.16	1739.8	1739.8	0.021	21.7	15.7	(160 222 29999)

Note: L_ω is the Nyquist limit from angular frequency; L_{k_x} is the Nyquist limit for k_x; L_{k_y} is the Nyquist limit for k_y; S_ω is the resolution in angular frequency; S_{k_x} is the resolution in k_x; S_{k_y} is the resolution in k_y; *Shape* reflects the dimensions of the resulting 2D+t frequency–wavenumber spectrum.

As the DIC recovered the surface elevation field from the observation of tracers that were on the free surface, the overall recovered elevation was dictated by the density and behaviour of the tracers. As the flow advected the tracers, the spatial density was not uniform and there were regions in the flow where the number of tracers was close to zero. At these locations, the DIC scheme did not successfully recover elevation information. Figure 5 demonstrates the proportion of pixels that were successfully recovered at each frame of the resulting video. These data were smoothed through the use of a Gaussian kernel density estimation (KDE) method (Weglarczyk, 2018). These values were normalized based on the maximum value of the distribution for all measurements. It can be observed that the spread of the KDE histograms increases as the flow rate increased over both bed types. The proportion of pixels with spatial information for measurements over the bed B has an intermediate peak value of around 0.5 for flow condition FC1B, whereas the proportion of pixels with spatial information for bed A tests decrease from FC1A to FC5A. The spread is defined by 'holes' that advected with the flow. These holes were not interpolated before the application of the discrete Fourier transform (DFT) and were set to 0 mm. However, if these non-complete DIC data could reconstruct robust frequency–wavenumber plots in the streamwise and lateral directions with sufficient fidelity to separate the different wave types, then this 3D surface elevation data may be used to investigate the nature of the free surface of turbulent flows.

3. Analysis of water surface level measurements

The identification of the different patterns (turbulence-forced and freely propagating gravity-capillary waves) on the surface of turbulent open-channel flows was achieved by means of the frequency–wavenumber spectrum. This method transforms the elevation at any location into a function of angular frequency $\omega = 2\pi f$ (where f is the frequency) and wavenumber vector $\boldsymbol{k}$

defined with:

$$\boldsymbol{k} = [k_x, k_y] \tag{1}$$

$$k = |\boldsymbol{k}| = 2\pi/\lambda \tag{2}$$

where λ is the wavelength and k_x and k_y are the wavenumber components in the streamwise and lateral directions respectively. This decomposition can be found from using a Fourier transform on the surface elevation $\zeta(x, y, t)$ in space (x, y) and in time t.

Due to physical parameters of the system such as the water depth, surface tension, gravity and the mean flow speed the propagation of waves at a given angular frequency is restricted to a finite amount of spatial wavelengths. The angular frequency at which waves propagate becomes a function of $\boldsymbol{k}$. The functional form of $\omega = \Omega(\boldsymbol{k})$ is called the dispersion relation. There are two functional forms of the dispersion relation for shallow turbulent open-channel flow: turbulence-forced fluctuations Ω_A and gravity-capillary waves Ω_{GW}, which are waves affected by surface tension of the fluid and gravity.

Turbulence-forced surface fluctuations are expected to move along the direction of the flow at a speed comparable to that of the turbulent disturbances that creates them (Teixeira & Belcher, 2006). If the mean surface velocity $\bar{U}_S$ of the flow is faster than pattern deformations, the fluctuations in time at a fixed point are primarily due to advection, yielding the following approximate dispersion relation for turbulence-forced fluctuations (Dolcetti et al., 2022):

$$\Omega_A(\boldsymbol{k}, \bar{\mathbf{U}}_\mathbf{S}) \approx \boldsymbol{k} \cdot \bar{\mathbf{U}}_\mathbf{S} \tag{3}$$

The dispersion relationship for gravity capillary waves in the absence of flow is:

$$\Omega_i(\boldsymbol{k}, d) = \boldsymbol{k}\sqrt{gd\frac{1 + B\tanh(kd)}{B}\frac{\tanh(kd)}{kd}} \tag{4}$$

where:

$$B = \frac{\rho g}{k^2 \gamma} \tag{5}$$

is the Bond number, γ is the surface tension, ρ is the density of water and d is the water depth. In terms of
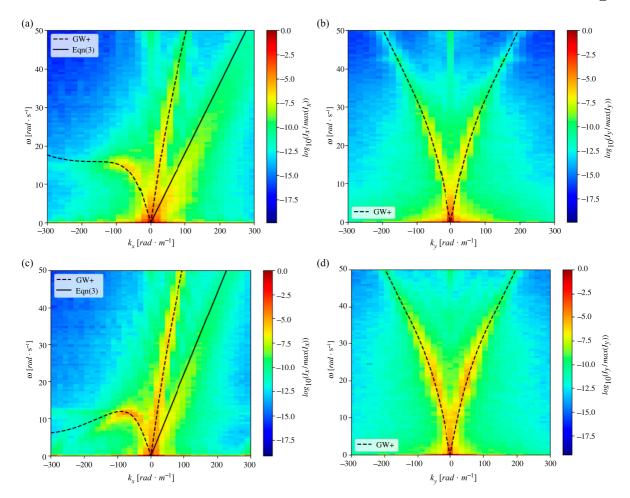
Figure 6. Frequency–wavenumber spectrum for (a) $k_y = 0$, (b) $k_x = 0$ for flow condition FC1A, (c) $k_y = 0$, and (d) $k_x = 0$ for flow condition FC1B (solid line relates to Equation (3), dashed line relates to Equation (7) with the $+$ sign, colour online).

the gravity-capillary wave dynamics, the vertical velocity profile in an open-channel flow can be approximated by a linear profile:

$$U(z) = \left(m\frac{z}{d} + (1 - m) \right) \bar{U}_s \quad (6)$$

This leads to the following explicit equation describing the dispersion relation of gravity-capillary waves in open-channel flows (Dolcetti et al., 2022; Lamb, 1945; Teixeira & Belcher, 2006):

$$\Omega_{GW}(\boldsymbol{k}, d, \bar{\mathbf{U}}_{\mathbf{S}}) = (1 - \beta)\Omega_A \pm \sqrt{(\beta\Omega_A)^2 + \Omega_i^2} \quad (7)$$

where:

$$\beta = \frac{m}{2}\frac{\tanh(kd)}{kd} \quad (8)$$

In this work, m in Equations (8) and (6) is set to 0.34 as in Dolcetti et al. (2022) because this value corresponds to a depth-averaged velocity to surface velocity index $\bar{U}_B / \bar{U}_s = 0.83$, which is a typical value for river and open-channel flows (Hauet et al., 2018). The positive square root solution is denoted GW+ and the negative square root solution is denoted GW–. GW+ can be further distinguished as GW+u and GW+d,
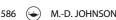
indicating waves propagating against and in the same direction of the flow, respectively (see Luo et al., 2023 for details).

3.1. Feature extraction method

This analysis yields a dispersion relation for turbulence-induced (forced) waves and dispersion relations for gravity-capillary waves. These relations can therefore describe the complex combination of different wave types on the free surface.

The frequency–wavenumber spectrum was obtained in 2D+t dimensions in order to identify the wave types that propagated in all directions. The underlying assumption is that the general motion of the free surface was well characterized by leading-order linear wave theory. If this assumption holds, it is possible using the frequency–wavenumber spectrum to recover the different dispersion relations (Dugan et al., 2001; Hauser et al., 2005; Krogstad & Trulsen, 2010).

Indicating as ζ_{mnp} the discrete representation of the free surface $\zeta(x, y, t)$ at a discrete location (x_m, x_n) $\tilde{m} \in [0, N_x - 1], n \in [0, N_y - 1]$ and time instance t_p $p \in [0, N_t - 1]$ with number of samples N_x, N_y, N_t in the x,
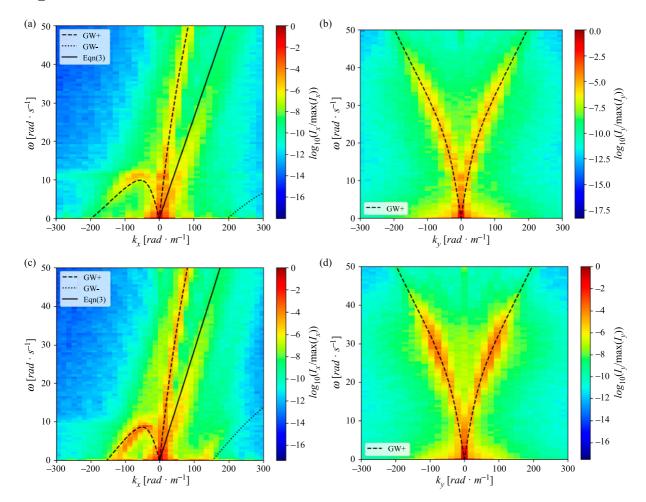
Figure 7. Frequency wavenumber spectrum for (a) $k_y = 0$, (b) $k_x = 0$ for flow condition FC2A, (c) $k_y = 0$, and (d) $k_x = 0$ for flow condition FC2B(solid line relates to Equation (3), dashed and dotted lines relate to Equation (7) with the $+$ sign and $-$ sign, respectively, colour online).

y and time dimension, respectively, the discrete three-dimensional discrete Fourier transform $\hat{\zeta}_{\chi\xi\tau}$ is:

$$\hat{\zeta}_{\chi\xi\tau} = \sum_{\tilde{m}=0}^{N_x-1} \sum_{n=0}^{N_y-1} \sum_{p=0}^{N_t-1} \zeta_{\tilde{m}np}$$

$$\times \exp\left[-i\left(\frac{2\pi}{N_x}\tilde{m}\chi + \frac{2\pi}{N_y}n\xi + \frac{2\pi}{N_t}p\tau\right)\right] \quad (9)$$

where $\chi = -N_x/2, \ldots, N_x/2 - 1$ and $\xi = -N_y/2, \ldots, N_y/2$ represent the spatial wavenumber through the relations:

$$k_x = \frac{2\pi\chi}{\Delta x N_x} \quad \text{and} \quad k_y = \frac{2\pi\xi}{\Delta y N_y} \quad (10)$$

and $\tau = 0, \ldots, N_t$ represents the frequency through the relation:

$$\omega = \frac{2\pi\tau}{\Delta t N_t} \quad (11)$$

The power spectrum I of the frequency–wavenumber spectrum, defined by:

$$I_{\chi\xi\tau} = \frac{1}{N_x N_y N_t}|\hat{\zeta}_{\chi\xi\tau}|^2 \quad (12)$$

was calculated for every 10 s (N_t therefore reduces to 1000) of DIC surface elevation data and then the results were averaged. This average power spectrum was later analysed.

The Nyquist limits (L_ω, L_{k_x} and L_{k_y}), the resolutions (S_ω, S_{k_x} and S_{k_y}) for ω, k_x and k_y, and the spectra dimensions are presented in Table 2. No window was used in the DFT analysis.

4. Results

Once the DIC system had completed its measurement and the water surface elevations were processed, the averaged power spectrum of the water surface was found for each experiment. This gave a spatial spectra for values of the wavenumbers in the streamwise (x) and lateral (y) direction. Two slices corresponding to $k_x = 0\,\text{rad}\,\text{m}^{-1}$ and $k_y = 0\,\text{rad}\,\text{m}^{-1}$ (named I_y and I_x) representing waves in the streamwise and the lateral direction, respectively, were selected for the presentation of the results. The selected slices were normalized by the maximum value observed in the slice.

Theoretical dispersion relations were obtained for the streamwise and the lateral directions from Equations (3) and (7) based on the measured depth and
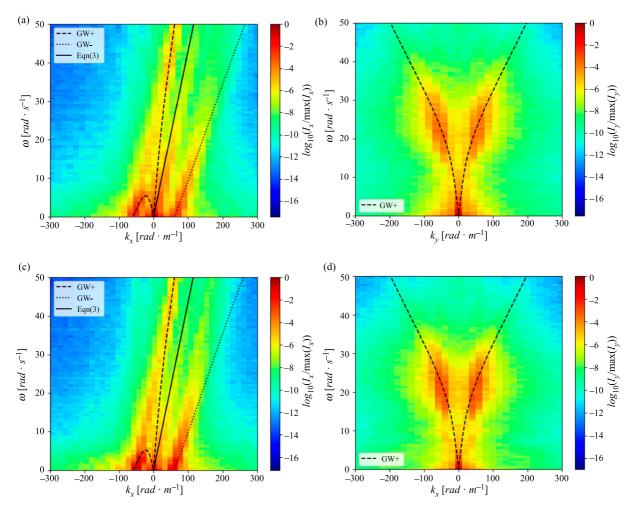
Figure 8. Frequency wavenumber spectrum for (a) $k_y = 0$, (b) $k_x = 0$ for flow condition FC3A, (c) $k_y = 0$, and (d) $k_x = 0$ for flow condition FC3B (solid line relates to Equation (3), dashed and dotted lines relate to Equation (7) with the $+$ sign and $-$ sign, respectively, colour online).

velocity reported in Table 1. In the lateral direction the time-averaged surface velocity was assumed to be zero as the channel cross-sectional shape was rectangular and the lateral slope was checked and found to be zero. The lines following the theoretical relationships were overlaid onto the results presented from the spectral analysis of the collected DIC data. This was done to discover whether the 2D+t spectral analysis of the DIC data could recover the relationships from the expected wave types.

Figures 6, 7, 8, 9, and 10 present the Fourier representation of the DIC recovery for the case where $k_x = 0$ rad m^{-1} and $k_y = 0$ rad m^{-1} for all the flow conditions outlined in Table 1. These figures clearly show the two types of waves that were expected.

The first type represents forced surface waves created by rising turbulent eddies impacting with the water surface. These features created significant deformations that propagated downstream at approximately the surface water velocity. This wave was always observed in all flow conditions over both beds (see Figures 6a,c, 7a,c, 8a,c, 9a,c, and 10a,c). The relative dominance of this type of wave decreased as water depth and flow velocity increased.

The second type of waves were gravity-capillary waves that propagated relative to the flow velocity in all directions. This results in two types of gravity-capillary waves: GW– waves, corresponding to the negative sign solution, and GW+ waves, corresponding to the positive sign solution. GW+ can be further spilt into waves with positive wavenumber (GW+d, downstream-propagating, $k_x > 0$) and negative wavenumber (GW+u, upstream-propagating, $k_x < 0$).

For FC1 and FC2 shown in Figures 6 and 7, respectively, two types of waves (GW+u and GW+d) can be clearly seen over both beds, with the pattern of GW+u waves differing over the two bed types in both the measured spectra and the theoretical relations shown in Figure 11. GW– waves were not observed at the FC1 flow condition in accordance with theory. In the test with the FC2 conditions a similar pattern was observed, with the appearance of GW– waves starting to occur at the zero-crossing at approximately $k_x = 120$ rad m^{-1}. So for flow condition FC1A, FC1B, FC2A and FC2B in Figures 6 and 7 there is good agreement for both the turbulent advection dispersion relation (Equation (3)) and the downstream gravity capillary
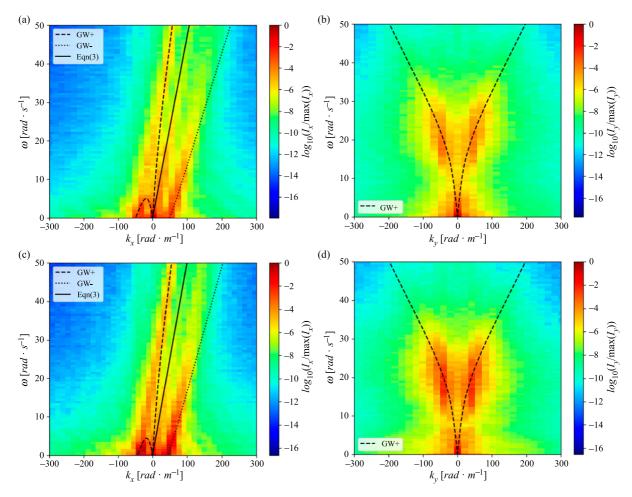
Figure 9. Frequency wavenumber spectrum for (a) $k_y = 0$, (b) $k_x = 0$ for flow condition FC4A, (c) $k_y = 0$, and (d) $k_x = 0$ for flow condition FC4B (solid line relates to Equation (3), dashed and dotted lines relate to Equation (7) with the + sign and − sign, respectively, colour online).

waves (Equation (7)) for wavenumbers larger than $0\,\text{rad}\,\text{m}^{-1}$. There is also good agreement for the negative wavenumber until less than $-100\,\text{rad}\,\text{m}^{-1}$, then the agreement decreases. For flow conditions FC3, the features of the advection and the downstream gravity capillary waves were less clear and there was not as distinct a separation from the advection and the gravity capillary waves as was seen in flow conditions FC1 and FC2.

In the tests with higher flow velocities and deeper water depths (FC3–FC5, see Figures 8, 9, and 10) a high-energy region to the left of the gravity waves dispersion relation seems to deviate from the theoretical curve. This region most likely indicates the presence of waves that propagate at an angle with respect to the direction of the flow, leading to an apparent deviation from theory. Similar patterns were observed in the 1D Fourier spectra by Dolcetti et al. (2016) and ascribed to radially uniform patterns of waves with the wavelength of stationary waves that could originate from non-linear interactions with the bed roughness and turbulence modes (Dolcetti & García Nava, 2019). Here, the appearance of these patterns in

the 2D spectra is most likely due to spectral leakage caused by the finite size of the measurements. In these tests the pattern in the positive wavenumber region is clearer, with the forced surface waves and the GW− and GW+d gravity waves clearly shown in FC3, FC4 and FC5.

For the recovery of the lateral waves (corresponding to the plane with $k_x = 0$), the agreement with the theoretical relationships is good throughout all the experiments. Although the frequency–wavenumber plots become less distinct as the flow rate got higher, the overall shape adheres well to the theoretical dispersion curve. The pattern of the results of this type of wave was similar over both beds.

In order to visualize the separation of the dispersion relation with respect to the change of the flow parameters, the dispersion relations calculated from the measured water depth and velocity for all flow conditions were presented in Figure 11. This figure shows that there is a clear separation in the streamwise direction over both beds, especially for the GW+u waves in the negative wavenumber. This difference is illustrated in the frequency–wavenumber
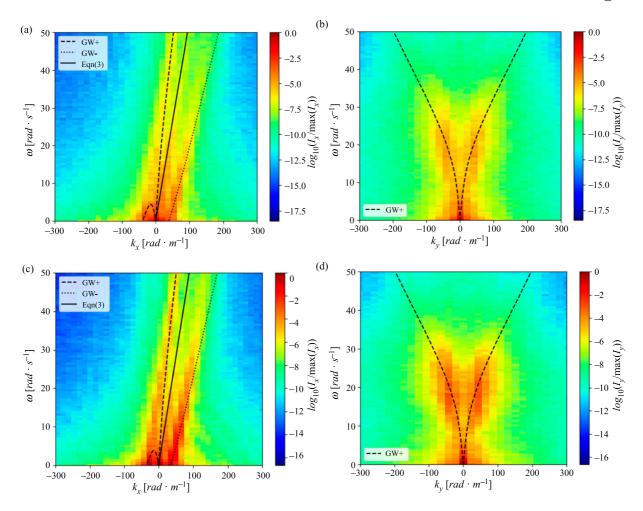
Figure 10. Frequency wavenumber spectrum for (a) $k_y = 0$, (b) $k_x = 0$ for flow condition FC5A, (c) $k_y = 0$, and (d) $k_x = 0$ for flow condition FC5B (solid line relates to Equation (3), dashed and dotted lines relate to Equation (7) with the + sign and − sign, respectively, colour online).

results in Figures 6a,b, and 7a,b. The measured pattern in the negative wavenumber region offers the potential that bed surface condition may be identified in flow conditions with low depths. The behaviour is mimicked in the lateral direction, although the change with respect to depth decays very quickly, with minimal separation in FC4 and FC5 for measurements over both beds in the negative wavenumber region.

The ability to separate out the gravity-capillary behaviour and the forced behaviour is an extremely powerful benefit of this approach. Discrimination of the streamwise dispersion relations allowed for the clear discrimination of different flow conditions over the flow range conditions in these experiments. Such a separation was carried out by the Fourier filtering method introduced by Luo et al. (2023). The method consists in applying a mask in Fourier space in order to eliminate all waves except the ones that satisfy a specific dispersion relation. Then, these waves are reconstructed in space-time through an inverse Fourier transform. An example of this separation is presented in Figure 12. It is important to note that the 2D+t spectra was used

in the masking. Figure 12 showcases the resulting separated flow structures for the forced waves and the gravity-capillary waves for FC1B and FC5B at an instant in time. The colourbar range in all these plots is twice the standard deviation of the water surface elevations of each particular wave type. The proposed flow conditions represent the two extremes of the experimental test range, nonetheless common features can be identified. It is clear that at both flow conditions, the 'typical' amplitude of the gravity-capillary waves are larger than the forced waves. This type of data presentation also allowed for an impression of the 3D nature of the waves, with all wave types showing a stronger coherence in the lateral rather than the streamwise direction. This figure presents the benefits in using a DIC-based approach, even if the 3D data obtained is sparse. There is the ability to successfully separate the components of the free surface which follow the forced dispersion relation and the components which follow the gravity-capillary relation. This separation allows for the potential to develop more detailed understanding of the physical causes of the individual wave types for a range of flow conditions.
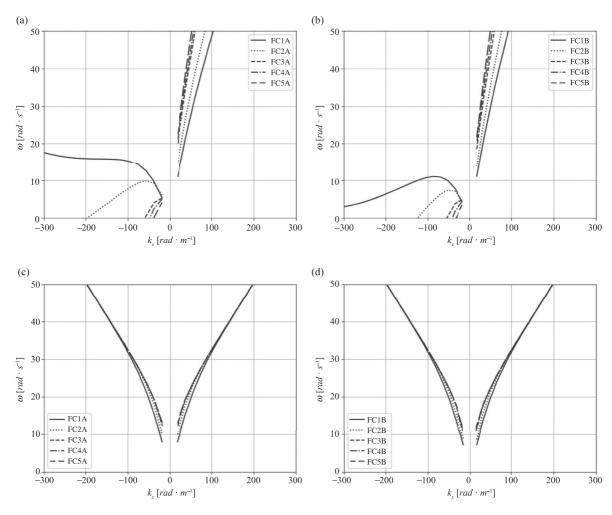
Figure 11. Comparison of the theoretical dispersion relation plots grouped by the bed type (A and B) for the range of experimental flow conditions FC1–FC5. In (a) the streamwise dispersion relations are shown for the A bed measurements, (c) contains the lateral dispersion relations for the A measurements. In (b) and (d) the B bed measurements with streamwise and lateral relations are presented, respectively.

5. Conclusion

The work reported in this paper investigated the capability of frequency–wavenumber analysis of free-surface data collected using DIC to describe the complex dynamic nature of free surface flows. DIC was selected as a measurement technique as it was able to remotely collect 3D water surface elevation data at a high spatial and temporal resolution. The DIC scheme was tested in a laboratory under various uniform and steady flow conditions over two beds with different surface topography. The DIC technique relied on particles that were placed in the flow and moved with the water surface. This characteristic, however, may cause some uncertainties in surface elevation reconstruction. In low flow conditions, the high density of particles could artificially reduce the amplitude of water surface deformations. In high flow conditions, instead, the lack of particles in regions of strong downwelling or surface divergence could lead to gaps in the measured surface distribution. These effects appeared to have limited impact on the derivation of frequency–wavenumber plots that were used to discriminate between different wave types.

The results presented in this work relate to the matching of the experimental frequency–wavenumber spectrum and the theoretical dispersion relations. Good matching and separation of different types of surface waves (forced and gravity-capillary and their sub-types) indicate that the reconstruction from the DIC derived data has good agreement to theoretical relations as well. The results show that gravity-capillary waves are present in flow conditions FC1 and FC2 over both beds, with this information captured in the dispersion relation. In the case of the streamwise frequency–wavenumber plots, as the flow rate increases (FC3 to FC5) the behaviour of the gravity-capillary waves appears to change substantially particularly in the negative wavenumber region. In the negative wavenumber region, the structure of the gravity-capillary waves becomes less distinct at the lower frequencies presumably due to noise. Streamwise and lateral frequency–wavenumber plots
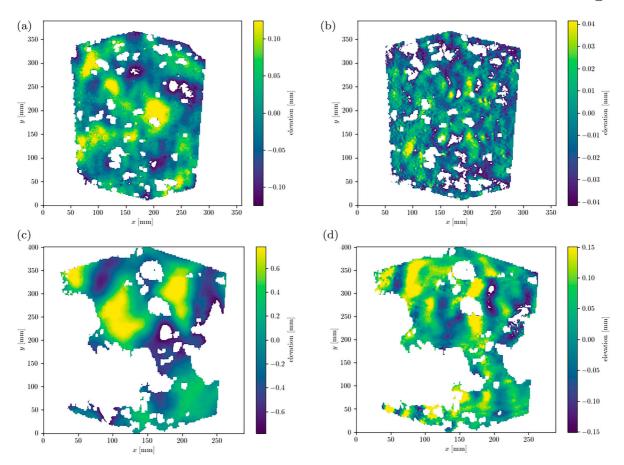
Figure 12. Extraction of the forced waves and the gravity-capillary waves using a mask centred at the forced dispersion relation. In (a) and (b) the gravity-capillary waves and the forced waves for FC1B, respectively, are shown. In (c) and (d) gravity-capillary waves and forced waves are presented for FC5B, respectively. Two standard deviations of the resulting masked free surface form the bounds of the colourbars.

reveal a systematic change in both forced and gravity waves. This validates the approach for the use of non-intrusive DIC-based systems to collect 3D data and analyse the free surface of shallow turbulent flows, even with the issue of missing data within the data sets.

Two beds with a similar scale – identical sphere diameters, but different arrangement – were used to examine whether frequency–wavenumber analysis of DIC water surface data could distinguish bed arrangement. An attempt was made at trying to maintain the same experimental flow conditions (Table 1) in order to investigate on the effect of the different bed layouts (FC1A and FC1B have a much larger difference in flow rate than the other flow conditions, though). In terms of the frequency–wavenumber spectra it was seen that the different bed conditions were indicated in the negative wavenumber region for FC1, FC2 and FC3. This suggests that the study of wave surface patterns for shallow flows could be used to distinguish bed topography especially at lower water depths.

The high level of agreement of the observed frequency–wavenumber values in comparison to the theoretical dispersion relations in addition to the 2D+t spectral reconstruction that the DIC measurement scheme produces allowed for a complete separation in space and time of the dispersion relations. This extraction allows the physical characteristics of these wave types to be quantified and visualized separately.

Data availability statement

The data used in this publication are available on the Zenodo platform at https://zenodo.org/records/13076686 and https://zenodo.org/records/16681767.

Disclosure statement

No potential conflict of interest was reported by the author(s).

Notation

A	cross-sectional liquid area (m^2)
A_R	aspect ratio (−)
d	water depth (m)
F	Froude number (−)
g	gravitational acceleration (m s^{-2})
$\boldsymbol{k}$	angular wavevector (rad m^{-1})
k_x	x−wavenumber component of $\boldsymbol{k}$ (rad m^{-1})
k_y	y−wavenumber component of $\boldsymbol{k}$ (rad m^{-1})
L_{k_x}	k_x Nyquist limit for (rad m^{-1})
L_{k_y}	k_y Nyquist limit (rad m^{-1})
L_ω	angular frequency Nyquist limit (rad s^{-1})
Q	discharge (m^3 s^{-1})
Re	Reynolds number (−)
S_{k_x}	k_x resolution (rad m^{-1})
S_{k_y}	k_y resolution (rad m^{-1})
S_ω	angular frequency resolution (rad s^{-1})
St	Stokes number (−)
$\bar{U}_B$	time- and depth-averaged streamwise velocity (m s^{-1})
$\bar{U}_S$	average streamwise surface velocity (m s^{-1})
W	flume width (m)
γ	surface tension (N m^{-1})
λ_x	wavelength in the streamwise direction (m)
λ_y	wavelength in the lateral direction (m)
ν	kinematic viscosity of water (m^2 s^{-1})
ρ	density of water (kg m^{-3})
ρ_{cs}	cenospheres density (kg m^{-3})
ω	angular frequency (rad s^{-1})
σ_{DIC}	free-surface elevation standard deviation measured via DIC (m)
σ_{DIC}	free-surface elevation standard deviation measured via conductivity probes (m)

ORCID

Fabio Muraro http://orcid.org/0000-0003-3843-2688
Simon J. Tait http://orcid.org/0000-0002-0004-9555

References

Akutina, Y. (2016). *Experimental investigation of flow structures in a shallow embayment using 3D-PTV* . McGill University (Canada).

Bouguet, J.-Y. (2000). Pyramidal implementation of the Lucas Kanade feature tracker description of the algorithm. http://sourceforge.net/projects/opencvlibrary/.

Brocchini, M., & Peregrine, D. (2001). The dynamics of strong turbulence at free surfaces. part 1. description. *Journal of Fluid Mechanics*, *449*, 225–254. https://doi.org/10.1017/S0022112001006012

Chu, T., Ranson, W., & Sutton, M. A. (1985). Applications of digital-image-correlation techniques to experimental mechanics. *Experimental Mechanics*, *25*(3), 232–244. https://doi.org/10.1007/BF02325092

Cobelli, P., Maurel, A., Pagneau, V., & Petitjeans, P. (2009). Global measurement of water waves by fourier transform profilometry. *Experiments in Fluids*, *46*(1), 1037–1047. https://doi.org/10.1007/s00348-009-0611-z

Dolcetti, G., & García Nava, H. (2019). Wavelet spectral analysis of the free surface of turbulent flows. *Journal of Hydraulic Research*, *57*(2), 211–226. https://doi.org/10.1080/00221686.2018.1478896

Dolcetti, G., Horoshenkov, K., Krynkin, A., & Tait, S. (2016). Frequency-wavenumber spectrum of the free surface of shallow turbulent flows over a rough boundary. *Physics of Fluids*, *28*(10), Article 105105. https://doi.org/10.1063/1.4964926

Dolcetti, G., Hortobágyi, B., Perks, M., Tait, S., & Dervilis, N. (2022). Using non-contact measurement of water surface dynamics to estimate river discharge. *Water Resources Research*. https://doi.org/10.1029/2022WR032829

Dolcetti, G., Krynkin, A., Alkmim, M., Cuenca, J., De Ryck, L., Sailor, G., Muraro, F., Tait, S. J., & Horoshenkov, K. V. (2024). Reconstruction of the frequency-wavenumber spectrum of water waves with an airborne acoustic Doppler array for noncontact river monitoring. *IEEE Transactions on Geoscience and Remote Sensing*, *62*, 1–14. https://doi.org/10.1109/TGRS.2024.3358672

Donelan, M. A., Drennan, W. M., & Magnusson, A. K. (1996). Nonstationary analysis of the directional properties of propagating waves. *Journal of Physical Oceanography*, *26*(9), 1901–1914. https://doi.org/10.1175/1520-0485(1996)026 < 1901:NAOTDP > 2.0.CO;2

Dugan, J., Piotrowski, C., & Williams, J. (2001). Water depth and surface current retrievals from airborne optical measurements of surface gravity wave dispersion. *Journal of Geophysical Research: Oceans*, *106*(C8), 16903–16915. https://doi.org/10.1029/2000JC000369

Ferguson, R. (2007). Flow resistance equations for gravel- and boulder-bed streams. *Water Resources Research*, *43*(5): W05427. https://doi.org/10.1029/2006WR005422

Fleet, D., & Weiss, Y. (2006). *Optical flow estimation* (pp. 237–257). Springer.

Fukami, K., Yamaguchi, T., Imamura, H., & Tashiro, Y. (2008). Current status of river discharge observation using non-contact current meter for operational use in Japan. In *World Environmental and Water Resources Congress 2008: Ahupua'A* (pp. 1–10). https://doi.org/10.1061/40976(316)278

Gakhar, S., Koseff, J. R., & Ouellette, N. T. (2020). On the surface expression of bottom features in free-surface flow. *Journal of Fluid Mechanics*, *900*(A41), 1–11.

Gharib, M., & Weigand, A. (1996). Experimental studies of vortex disconnection and connection at a free surface. *Journal of Fluid Mechanics*, *321*, 59–86. https://doi.org/10.1017/S0022112096007641

Guidi, G., Russo, M., & Angheleddu, D. (2014). 3D survey and virtual reconstruction of archeological sites. *Digital Applications in Archaeology and Cultural Heritage*, *1*(2), 55–69. https://doi.org/10.1016/j.daach.2014.01.001

Hauet, A., Morlot, T., & Daubagnan, L. (2018). Velocity profile and depth-averaged to surface velocity in natural streams: A review over alarge sample of rivers. In *E3s Web of Conferences* (Vol. 40, p. 06015). EDP Sciences.

Hauser, D., Kahma, K., Krogstad, H. E., Lehner, S., Monbaliu, J. A. J., & Wyatt, L. (2005). *Measuring and analysing the directional spectra of ocean waves*. Office for Official Publications of the European Communities.

Jähne, B., Klinke, J., & Waas, S. (1994). imaging of short ocean wind waves: A critical theoretical review. *Journal*

of the Optical Society of America A, *11*(8), 2197–2209. https://doi.org/10.1364/JOSAA.11.002197

Krogstad, H. E., & Trulsen, K. (2010). Interpretations and observations of ocean wave spectra. *Ocean Dynamics*, *60*(4), 973–991. https://doi.org/10.1007/s10236-010-0293-3

Lamb, H. (1945). *Hydrodynamics*. Dover Publications.

Luo, Q., Dolcetti, G., Stoesser, T., & Tait, S. (2023). Water surface response to turbulent flow over a backward-facing step. *Journal of Fluid Mechanics*, *966*, A18. https://doi.org/10.1017/jfm.2023.350

Muraro, F. (2024). *Hydrodynamics over Permeable Beds* [PhD thesis]. University of Sheffield.

Muraro, F., Dolcetti, G., Nichols, A., Tait, S. J., & Horoshenkov, K. V. (2021). Free-surface behaviour of shallow turbulent flows. *Journal of Hydraulic Research*, *59*(1), 1–20. https://doi.org/10.1080/00221686.2020.1870007

Nichols, A., Rubinato, M., Cho, Y.-H., & Wu, J. (2020). Optimal use of titanium dioxide colourant to enable water surfaces to be measured by Kinect Sensors. *Sensors*, *20*(12), 3507. https://doi.org/10.3390/s20123507

Nichols, A., Tait, S., Horoshenkov, K., & Shepherd, S. (2013). A non-invasive airborne wave monitor. *Flow Measurement and Instrumentation*, *34*, 118–126. https://doi.org/10.1016/j.flowmeasinst.2013.09.006

Nichols, A., Tait, S. J., Horoshenkov, K. V., & Shepherd, S. J. (2016). A model of the free surface dynamics of shallow turbulent flows. *Journal of Hydraulic Research*, *54*(5), 516–526. https://doi.org/10.1080/00221686.2016.1176607

Pan, B. (2011). Recent progress in digital image correlation. *Experimental Mechanics*, *51*(7), 1223–1235. https://doi.org/10.1007/s11340-010-9418-3

Pan, B. (2018). Digital image correlation for surface deformation measurement: Historical developments, recent advances and future goals. *Measurement Science and Technology*, *29*(8), Article 082001. https://doi.org/10.1088/1361-6501/aac55b

Pan, B., Qian, K., Xie, H., & Asundi, A. (2009). Two-dimensional digital image correlation for in-plane displacement and strain measurement: A review. *Measurement Science and Technology*, *20*(6), Article 062001. https://doi.org/10.1088/0957-0233/20/6/062001

Peters, W., & Ranson, W. (1982). Digital imaging techniques in experimental stress analysis. *Optical Engineering*, *21*(3), 427–431. https://doi.org/10.1117/12.7972925

Robert, A. (1990). Boundary roughness in coarse-grained channels. *Progress in Physical Geography*, *14*(1), 42–70. https://doi.org/10.1177/030913339001400103

Savelsberg, R., & Van De Water, W. (2009). Experiments on free-surface turbulence. *Journal of Fluid Mechanics*, *619*, 95–125. https://doi.org/10.1017/S0022112008004369

Smeltzer, B. K., Æsøy, E., & Ellingsen, S. Å. (2019). Observation of surface wave patterns modified by sub-surface shear currents. *Journal of Fluid Mechanics*, *873*, 508–530. https://doi.org/10.1017/jfm.2019.424

Smolentsev, S., & Miraghaie, R. (2005). Study of a free surface in open-channel water flows in the regime from "weak" to "strong" turbulence. *International Journal of Multiphase Flow*, *31*(8), 921–939. https://doi.org/10.1016/j.ijmultiphaseflow.2005.05.008

Teixeira, M., & Belcher, S. (2006). On the initiation of surface waves by turbulent shear flow. *Dynamics of Atmospheres and Oceans*, *41*(1), 1–27. https://doi.org/10.1016/j.dynatmoce.2005.10.001

Tropea, C., Yarin, A. L., & Foss, J. F. (2007). *Springer handbook of experimental fluid mechanics* (Vol. 1). Springer.

Tsubaki, R., & Fujita, I. (2005). Stereoscopic measurement of a fluctuating free surface with discontinuities. *Measurement Science and Technology*, *16*(10), 1894–1902. https://doi.org/10.1088/0957-0233/16/10/003

Turney, D. E., Anderer, A., & Banerjee, S. (2009). A method for three-dimensional interfacial particle image velocimetry (3d-ipiv) of an air–water interface. *Measurement Science and Technology*, *20*(4), Article 045403. https://doi.org/10.1088/0957-0233/20/4/045403

Vandenberghe, S., D'Asseler, Y., Van de Walle, R., Kauppinen, T., Koole, M., Bouwens, L., K. Van Laere, Lemahieu, I., & Dierckx, R. (2001). Iterative reconstruction algorithms in nuclear medicine. *Computerized Medical Imaging and Graphics*, *25*(2), 105–111. https://doi.org/10.1016/S0895-6111(00)00060-4

Walsh, E., Hancock III, D., Hines, D., Swift, R., & Scott, J. (1985). Directional wave spectra measured with the surface contour radar. *Journal of Physical Oceanography*, *15*(5), 566–592. https://doi.org/10.1175/1520-0485(1985)015 < 0566:DWSMWT > 2.0.CO;2

Weglarczyk, S. (2018). Kernel density estimation and its application. In *ITM Web of Conferences* (Vol. 23, p. 00037). EDP Sciences.

Welber, M., Le Coz, J., Laronne, J. B., Zolezzi, G., Zamler, D., Dramais, G., Hauet, A., & Salvaro, M. (2016). Field assessment of noncontact stream gauging using portable surface velocity radars (svr). *Water Resources Research*, *52*(2), 1108–1126. https://doi.org/10.1002/wrcr.v52.2

Wu, J., Nichols, A., Krynkin, A., & Croft, M. (2022). Digital image correlation for stereoscopic measurement of water surface dynamics in a partially filled pipe. *Acta Geophysica*, *70*(5), 2451–2467. https://doi.org/10.1007/s11600-022-00792-w